A Fully Optoelectronic Continuous-Wave 2-Port Vector Network Analyzer Operating From 0.1 THz to 1 THz

ANUAR D. J. FERNANDEZ OLVERA ⬡, AMLAN K. MUKHERJEE ⬡, AND SASCHA PREU ⬡

(Regular Paper)

Department of Electrical Engineering and Information Technology, TU Darmstadt, 64283 Darmstadt, Germany

CORRESPONDING AUTHOR: Anuar D. J. Fernandez Olvera (e-mail: fernandez@imp.tu-darmstadt.de).

ABSTRACT We present a 2-port terahertz vector network analyzer (VNA) based on four continuous-wave (CW) photomixers and a pair of telecom-wavelength CW lasers. The presented optoelectronic VNA is free-space coupled and can operate continuously from 0.1 THz to 1 THz with a resolution of 2 MHz. We demonstrate two different applications with it: the determination of the material properties of a quartz wafer and the characterization of a terahertz distributed Bragg reflector (DBR).

INDEX TERMS ErAs:In(Al)GaAs photoconductors, terahertz, optoelectronics, vector network analyzer.

I. INTRODUCTION

In recent years, the development of terahertz and sub-terahertz measurement systems using photonic and optoelectronic architectures has gained relevance within the terahertz research community. Their frequency coverage of several octaves, lower cost, and in some cases, much better frequency accuracy, has made them an interesting option for research and industry.

The core of these optoelectronic systems are the photomixers that generate and coherently detect the reference terahertz waves required to perform the measurements. They convert an optical beatnote resulting from the mixing of two (or more) laser tones having a difference frequency equal to the desired terahertz frequency to be generated [1]. Since lasers can easily be tuned to exhibit any frequency difference between zero and several THz, the only limitation in frequency coverage is imposed by the carrier dynamics in the photomixer [2]. Still, bandwidths exceeding 6.5 THz have been demonstrated with telecom-wavelength lasers in pulsed systems and beyond 4 THz [3], [4] in continuous-wave (CW) systems [5]. The use of telecom-wavelength lasers makes the opotelectronic systems even less expensive, and allows to implement sophisticated systems with advanced capabilities, such as optical frequency combs, which enable Hz-level terahertz linewidths and resolution [6], [7]. Indeed, there are already photomixer-based

terahertz spectrum analyzers exploiting such advanced capabilities able to measure over several sub-terahertz and terahertz bands with a Hz resolution [8], [9].

Regarding vector network analyzers (VNAs), three photomixer-based architectures have been reported recently: two 1.5-port versions covering from 0.15 THz to 3 THz [10], [11] and a 2-port version covering from 0.2 THz to 2 THz [12]. These systems used a femtosecond pulsed laser to drive the photomixers, which means that the generated terahertz signal used for the measurements is also a pulse, composed of several thousands of frequency components [7]. The advantage of this architecture is that it allows to perform extremely broadband measurements relatively fast. Its disadvantages are that it requires a mechanical delay stage to operate, which involves the use of bulky free-space optics, and its limited frequency resolution, which is no better than a few GHz.[1]

If the VNA is used to measure linear devices or materials with a relatively broad spectral response, the aforementioned

---

[1]These two issues are very related. The mechanical stage is employed to delay a copy of the optical pulse used for terahertz generation. The delayed optical pulse then 'interferes' with the terahertz pulse in the receiving photomixer, and the resulting 'interferogram' is Fourier transformed to get the spectrum. Thus, the resolution depends on the time interval covered with the stage.

disadvantages are no noteworthy limitations. However, if the VNA is used to measure devices or materials with narrow resonances, the resolution may be insufficient [13]. Further, the simultaneous presence of thousand of different frequency components might become problematic when measuring non-linear terahertz components, like transistors, mixers or simple receiver diodes. For these reasons, the architectures that have been used to characterize actual terahertz components have predominantly been based on electronic CW VNAs [14], [15]. However, they have only offered a frequency coverage of 0.01-0.325 THz using 3 different frequency extenders [14] and of 0.325-0.75 THz using 2 frequency extenders [15].

In this article, we demonstrate a free-space optoelectronic VNA based on CW photomixers covering from 0.1 to 1 THz. The implementation presented here is considerably simpler than pulsed photomixer-based architectures, since it does not require a femtosecond pulsed laser or a mechanical delay stage to operate. Moreover, it exhibits around three orders of magnitude improved frequency resolution. Although we only demonstrate free-space measurements, this implementation can be right away employed to characterize transmission-line coupled terahertz components when used in conjunction with the schemes proposed in [14], [15]. To the knowledge of the authors, this is the first demonstration of a CW 2-port VNA operating continuously between 0.1 and 1 THz.

The architecture of the implemented VNA is described in detail in Section II. The calibration procedure used to perform the measurements, as well as the definition of the measurement parameters are presented in Section III. Two different applications of two different measurements performed with the VNA are shown in Section IV. In the first one, we use the amplitude information obtained with the two ports to determine the material properties of a quartz wafer between 0.1 GHz and 1 THz. In the second one, we use the amplitude and the phase information measured with the two ports to get a detailed characterization of a distributed bragg reflector (DBR) between 0.58 and 0.74 THz. Finally, some concluding remarks and future applications of the implemented VNA are discussed in Section V.

II. SYSTEM ARCHITECTURE

A schematic representation of the VNA architecture is shown in Fig. 1. Like any VNA, it consists of three main components: the transmitters (Tx1 and Tx2), the receivers (Rx1 and Rx2), and the test sets [16]. Both transmitters and receivers are photomixers driven by a single photonic unit, which ensures phase locking and excellent relative phase stability [17]. Such homodyne architecture does not impede the simultaneous acquisition of amplitude and phase information, as demonstrated in [18], [19]. However, unlike in electronic VNA architectures, no reference receivers are employed. The amplitude stability is only guaranteed by the power stability in the lasers, measured to be better than 0.2 dB. The test sets are free-space coupled, composed of wire-grid polarizers (WGPs). This allows us to overcome the frequency limitations imposed by transmission-line coupled test sets that are typically narrow
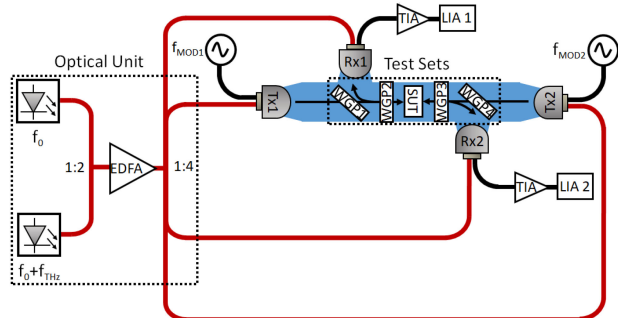

FIGURE 1. Schematic diagram of the VNA architecture.

band, which in turn allows us to exploit the extremely wide-band performance of the photomixers for the measurements.

In the following subsections, we describe the specific details and working principles of each of the components of the architecture.

A. PHOTONIC UNIT

The photonic unit consists of a pair of telecom-wavelength DFB lasers from TOPTICA photonics [20], whose temperature and current are tuned to achieve a defined frequency offset equal to the terahertz frequency to be generated f_{THz}. The two lasers signals are combined by a 1:2 fiber coupler, and subsequently amplified by an Erbium Doped Fiber Amplifier (EDFA) up to to 120 mW. Afterwards, a 1:4 splitter is used to distribute the laser signals to the two photomixing transmitters and the two photomixing receivers.

B. TERAHERTZ TRANSMITTERS AND RECEIVERS

The transmitters, henceforth Tx1 and Tx2, are commercial telecom-wavelength PIN photodiodes with an integrated bow-tie antenna attached to a silicon lens, similar to the one in [20]. They are both associated to port 1 and port 2 simultaneously, and they are both driven by the signal generated by the photonic unit. The intensity of such signal can be expressed as [1]

$$I_{OPT}(t) = I_0 + I_0 \cos(2\pi f_{THz} t) \qquad (1)$$

I_0 being is the average optical intensity of the lasers. The photodiodes absorb this optical power at a rate proportional to $I_{OPT}(t)$, resulting in the generation of electron-hole pairs at a terahertz rate. The photo-excited electron-hole pairs are separated by the built-in field of the photodiodes and by any additional DC bias, giving rise to a DC current and an AC current with frequency f_{THz}. The AC terahertz photocurrent is then radiated by the bow-tie antenna attached to the photo-diode, resulting in an emitted field E_{THz}.

The linewidth of the emitted field, and therefore the frequency resolution of the VNA, depends entirely on the linewidth of the DFB lasers. Measurements with a terahertz spectrum analyzer have shown a 3-dB linewidth of 2 MHz [17]. This is therefore the highest resolution of the VNA.

Following emission, E_{THz} is subsequently guided by the free-space coupled test sets to both receivers, after going through the sample under test (SUT).

The receivers, henceforth Rx1 and Rx2, associated to port 1 and 2, respectively, are two telecom-wavelength compatible ErAs:InGaAs photoconductors with an integrated antenna attached to a silicon lens. They are similar to the ones described in [21]. Both PCAs are driven by the same photonic signal used for generation in Tx1 and Tx2, hence the homodyne nature of the architecture. As in the case of the transmitters, the optical signal excites electron-hole pairs at a rate given by $I_{OPT}(t)$, resulting in a net local oscillator (LO) carrier density n_{LO} of

$$n_{LO} \sim I_0 + I_0\eta(f)\cos(2\pi f_{THz}t + \phi). \qquad (2)$$

where ϕ represents the phase difference between the optical beat note arriving at the receiver and the terahertz signal generated by the photodiodes after propagating through the test sets, the sample and all other components, and η represents the frequency-dependent lifetime roll-off due to the carrier dynamics of the photoconductor [1]. The received terahertz field, $E_{THz,P}$, transmitted or reflected by the sample under test (SUT), then biases the photoconductor. Such applied bias separates electrons from holes, resulting in the generation of a steady current i_{DET}, given by

$$i_{DET} \sim n_{LO}E_{THz,P}. \qquad (3)$$

Ultimately, only the DC term can be read out by the post-detection electronics, which is composed of a transimpedance amplifier (TIA) with a transimpedance gain of 10^6 and a lock-in amplifier. Therefore, we can rewrite i_{DET} as

$$i_{DET} \sim E_{THz,P}\cos(\phi). \qquad (4)$$

Where the phase is given by

$$\phi = \frac{2\pi f_{THz}d_0}{c_0} \qquad (5)$$

c_0 being the speed of light and d_0 the equivalent free-space path length difference between the received terahertz signal and the photonic LO. This means that when we sweep f_{THz}, we get a sinusoidal signal whose amplitude is proportional to $E_{THz,P}$ and whose frequency is proportional to ϕ. With the help of the Hilbert transform [18], we can acquire the amplitude and the phase information simultaneously without the need of a delay line or an explicit phase sweep.

In order to differentiate between the detected signals coming from Tx1 and Tx2, the bias of applied to each of the photodiodes is modulated at a different frequency, namely f_{MOD1} and f_{MOD2}, respectively. After amplification by the TIA, the two modulated signals detected in each of the receivers are demodulated by two lock-in amplifiers (LIAs) with dual demodulators. LIA1 demodulates the signals received by Rx1, while LIA2 demodulates the signals received by Rx2.
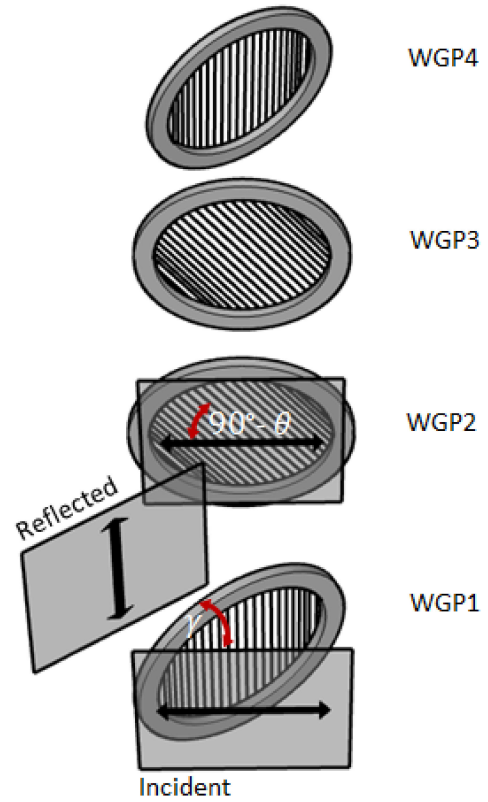

FIGURE 2. Graphical representation of two WGP-based directional couplers composing the two test sets of the VNA. The first directional coupler shows the polarization of the incident and reflected terahertz field. The SUT is mounted between WGP2 and 3.

C. TEST SETS

The splitting and coupling of the emitted terahertz signal into each of the receivers is done by WGPs acting as free-space directional couplers.

Two identical directional couplers are used in this architecture. Each of them is composed of two WGPs. The polarization axis of the first WGP (WGP1 or WGP4 in Fig. 1 and Fig. 2, depending on the propagation direction) in each of the directional couplers is aligned to polarization of the beam emitted by the nearest transmitting antenna (the polarization of the beam emitted by Tx1 is aligned to WGP1 polarization, while the polarization of the beam emitted by Tx2 polarization is aligned to WGP4 polarization). Hence, it transmits the emitted power with negligible loss. This WGP is placed with a tilt angle γ with respect to the wavefront of the emitted terahertz beam so that the signal reflected from the SUT can be directed to the first receiver. However, for this to occur, the polarization of the terahertz beam has to be rotated first. This is done with a second WGP (WGP2 or WGP3 in Fig. 1, depending on the propagation direction), whose polarization axis is placed with angle θ with respect to the polarization of the emitted beam. Similarly, the beam transmitted by the SUT, whose polarization has been rotated by the second and the third WGP (WGP2 and WGP3 in Fig. 1 and Fig. 2), is directed to the second receiver by the last WGP (WGP1 or WGP4 in
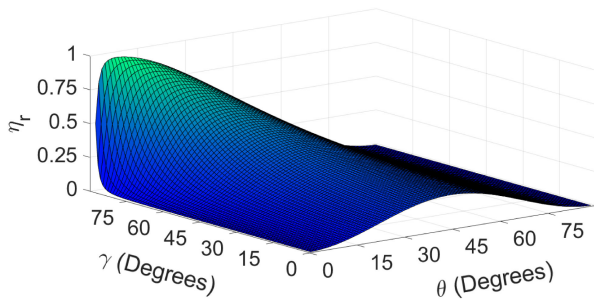
FIGURE 3. Fraction of incident terahertz power effectively directed to the terahertz receivers as a function of γ and θ.

FIGURE 4. 3D model of the calibration tool used to perform the measurements.

Fig. 1 and Fig. 2, depending on the propagation direction). Please note that the angle between the polarization axis of the tiled WGPs and the polarization axis of non-tilted WGPs is not θ but its projection on the plane of the tilted WGPs, which we denominate α.

If both directional couplers have the same configuration, as shown in Fig. 2, the fraction of terahertz power emitted by Tx1 (Tx2) reaching Rx2 (Rx1) when no sample is present η_r is given by

$$\eta_r = \cos^2(\theta)\left(1 - \cos^2(\alpha)\right) \qquad (6)$$

where

$$\alpha = \arctan\left(\frac{\sin(\theta)}{\cos(\theta)\cos(\gamma)}\right). \qquad (7)$$

Similarly, the fraction of the terahertz power emitted by Tx1 (Tx2) reaching Rx1 (Rx2) when a perfect mirror is used a sample is also given by (6).

The fraction of terahertz power that is not received by any of the receivers η_n is given by

$$\eta_n = 1 - \cos^2(\theta) + \cos^2(\theta)\cos^2(\alpha). \qquad (8)$$

Fig. 3 shows the fraction of the terahertz power reaching either of the receivers in the case of total transmission or total reflection as function of θ and γ. The optimum performance is achieved for high values of γ and for values of θ that range between $20°$ and $40°$. In a real setup, however, the maximum value that γ can take is limited by the surface area of the WGPs. For the architecture implemented here γ was set $\sim 45°$ and θ to $\sim 35°$. This results in a value of 0.33 for η_r, and a value of 0.66 for η_n.

An important issue is that the free-space coupling between the WGPs creates several undesired reflections and scattering, as it will become evident in Section IV. However, proper signal processing can partly remove their effects.

III. CALIBRATION AND DEFINITION OF MEASUREMENT PARAMETERS

We use the TTN self-calibration method proposed in [22] for broadband free-space measurements, which actually measures the sample to perform the calibration. This calibration method is the same as the one used in the pulsed-photomixer-based VNAs [11], [12]. The key idea behind this calibration method
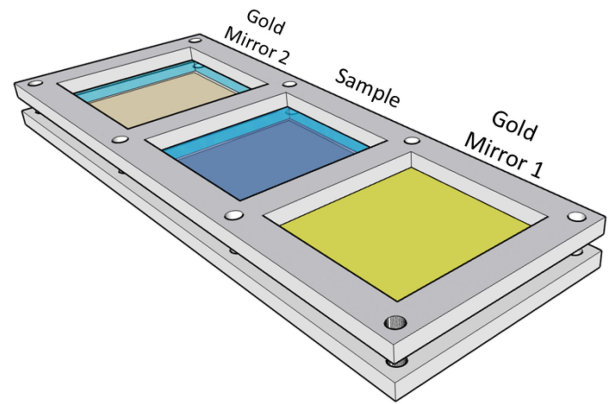
is the determination of a reference phase by means of a broadband measurement. The determination of a reference amplitude is rather trivial.

As indicated by (5), for the case of a transmission measurement, the phase in an empty VNA is completely determined by d_0: the path length difference between $E_{THz,P}$ and the optical local oscillator. By measuring over several frequency points, it is possible to determine its value very precisely, given that the periodicity of the phase will only be dependent on d_0. This value of d_0 can then be used as a reference to determine the change in path length, or phase, introduced by the SUT.

For a reflection measurement, a gold mirror is placed in the same plane as the SUT in order to obtain the reference phase. It is very important that the gold mirror is placed in the exact same position as the SUT, since the gold mirror actually represents a physical reference plane. To this end, we have designed the calibration tool shown in Fig. 4. This calibration tool is mounted on an optical rail, and it allows to position two gold mirrors exactly in the same position as the SUT, one for the reflection calibration measurement of each port. The gold mirrors are actually composed of a 0.725 μm layer of evaporated gold on a 220 μm quartz substrate. The SUT and the gold mirrors are kept in the same position by the mechanical force exerted by the screws that hold the tool together. This calibration method also works, to a certain degree, for samples thicker than the gold mirrors. In fact, we have used it for the measurement of the terahertz DBR, with a total thickness of 1830 μm. One just needs to introduce spacers between the gold mirrors and the calibration tool. The purpose of the spacers is to make sure that the gold mirrors and the SUT get all the same height, and hence lie on in the same reference plane. This is easier to achieve with spacers than can be compressed such as paper or rubber, since the mechanical force exerted by the screws of the tool could break the gold mirrors if rigid spacers are used.

Hence, the self-calibration procedure consists of four measurements:

1) an empty setup in which both reference transmission measurements are recorded: one for port 1 and one for port 2.
2) the first gold mirror as a SUT in which the reference reflection measurement for port 1 is recorded.
3) the second gold mirror as a SUT in which the reference reflection measurement for port 2 is recorded.
4) the four scattering parameters of the SUT are recorded.

We note that we measure the four scattering parameters of the SUT simultaneously in order to reduce the measurement time. This is also done in [12], and it has shown to render accurate results as the terahertz signals generated by Tx1 and Tx2 are modulated at different frequencies[2]. We use the usual definition for the scattering parameters:

1) S_{11} is the field reflection coefficient for the excitation signal generated by Tx1 (measured by Rx1).
2) S_{21} is the field transmission coefficient for the excitation signal generated by Tx1 (measured by Rx2).
3) S_{22} is the field reflection coefficient for the excitation signal generated by Tx2 (measured by Rx2).
4) S_{12} is the field reflection coefficient for the excitation signal generated by Tx2 (measured by Rx1).

IV. EXEMPLARY MEASUREMENT RESULTS

We performed two different measurements with the implemented optoelectronic VNA, each targeting a different application. In the first one, we measure the amplitude of the four scattering parameters of a quartz wafer in order to determine its refractive index and its thickness. This was done for the frequency range comprised between 0.095 THz and 1 THz using a frequency resolution of 20 MHz, although the signal processing algorithms used in the measured data reduced the usable frequency range to 0.1-0.9 THz. The results are presented in subsection A.

For the second application, we perform a characterization of an in-house fabricated terahertz DBR between 0.55 THz and 0.765 THz using also a frequency resolution of 20 MHz, although the signal processing algorithms used in the measured data reduced the usable frequency range to 0.57-0.75 THz. A broadband characterization of the amplitude response of the same DBR was already done with the pulsed-photomixer-based VNA demonstrated in [12]. The characterization performed here, however, also includes the phase response and has a 360 times better resolution. The results are presented in subsection B.

Fig. 5 shows the reference measurements required for the determination the scattering parameters for each of the measured samples, as specified in the calibration procedure described in Section III. They were measured after setting f_{MOD1} in Tx1 to 13.999 kHz, f_{MOD2} in Tx2 to 111.111 kHz, and

FIGURE 5. Magnitude of the reference measurements used for the determination of each of the scattering parameters. (a) Magnitude of the detected terahertz signal emitted by Tx1 and detected by Rx1 when a gold mirror was placed instead of the SUT, used for S11. (b) Magnitude of the detected terahertz signal emitted by Tx1 and detected by Rx2 for an empty setup, used for S21. (c) Magnitude of the detected terahertz signal emitted by Tx2 and detected by Rx2 when a gold mirror was placed instead of the SUT, used for S22. (d) Magnitude of the detected terahertz signal emitted by Tx2 and detected by Rx1 for an empty setup, used for S12.

by using an 8th-order low-pass filter with a time constant of 100 ms (corresponding to a noise equivalent bandwidth of 0.5 Hz) for the demodulation of each the four detected signals in the lock-in amplifiers.

These reference measurements give us a good indication of the maximum dynamic ranges that can be achieved with the implemented VNA, which are around 85 dB, 75 dB, 90 dB and 80 dB for S11, S21, S22 and S12, respectively. Although these dynamic ranges were achieved at 0.1 THz, the dynamic ranges

---

[2]Since the linewidth of the generated terahertz signals is around 2 MHz, even after modulating the two photodiodes with two distinct frequencies that differ by few tens of kHz, as it is the case here, the generated signals might overlap. However, due to the homodyne nature of the setup it is possible to perfectly recover each of the modulated signals, because, in practice, what the receivers see is an ultra-narrow linewidth signal.
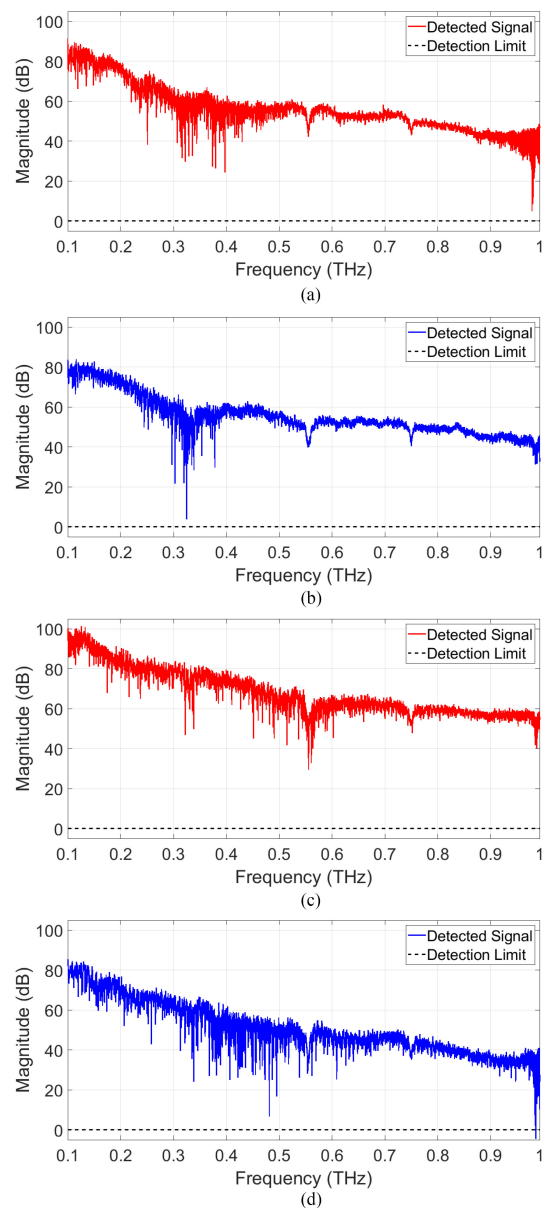
at 1 THz indicate that there is sufficient margin to increase the measurement range towards higher frequencies, or alternatively, to reduce the time constant used in the LIA demodulation. However, the attainment of these dynamic ranges in a real measurement depends strongly on the amount of undesired reflections generated between the sample to be measured and the WGPs. The effect of those undesired reflections is also evident in the reference measurements of Fig. 5, in particular for the range comprised between 0.3 and 0.5 THz. Still, it is possible to measure scattering parameters with values as low -60 dB for frequencies as high as 0.66 THz using the right post-processing techniques, as we will show next.

A. APPLICATION 1: DETERMINATION OF MATERIAL PROPERTIES

Using the lock-in amplifier settings specified before, and the already described calibration technique, we obtained the four scattering parameters of a z-cut quartz wafer (non-birefringent) with a nominal thickness of 220 μm. In order to reduce the artifacts produced by the unwanted reflections between the different components in the setup, we applied a finite-impulse response (FIR) low-pass filter to the measured data to remove any components that were outside the spectrum of the signal of interest. There are different approaches to obtain such spectrum. One of them is to use the eigenvalue decomposition on the autocorrelation matrix of the measured data. Another one, much simpler, is to use the discrete Fourier transform (DFT) on the measured data. We use the latter here. This allows us to determine the passband required to remove the components outside the spectrum of interest. We remark that this approach is equivalent to time-gating, since the filtering, performed directly in the data measured in the frequency domain, can be seen as a selective windowing in the time domain.

To achieve an optimal performance, the band-pass filtering is implemented in two steps. First, the measured data is decimated by a factor of two to reduce its length. This has a two-fold effect: it performs an initial low-pass filtering, and it reduces the order of the actual low-pass filter applied to the measured data. Then, the low-pass filter is applied to the decimated data. Finally, the data is interpolated and expanded to its original length. The outcome of such procedure on the four scattering parameters obtained from the measured data is shown in Fig. 6. Please note that the maximum measured reflection coefficient was -60 dB, obtained at 0.66 THz. Ideally, a similar value should have been achieved at 0.33 THz. However, the increased presence of undesired reflections between 0.3-0.5 THz made it more difficult for the post-processing filtering to discriminate between those and the ones coming from the quartz wafer.

Fig. 6 also shows a comparison with the theoretical scattering parameters that would be obtained from a sample with the thickness and the refractive index estimated using the filtered data. Both parameters are estimated by fitting the squared magnitude of the ratio between the measured transmission coefficient and the measured reflection coefficient to the squared
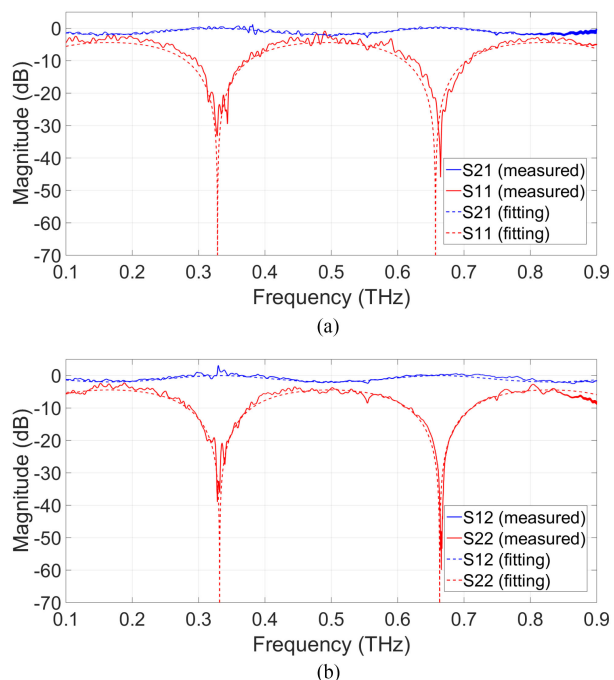

FIGURE 6. Comparison between the magnitude of the measured scattering parameters of the 220 μm quartz wafer after the filtering process, and the theoretical amplitude of the scattering parameters calculated using the fitted values. (a) Comparison obtained for port 1. (b) Comparison obtained for port 2.

magnitude of theoretical ratio s that would be exhibited by a piece of dielectric slab with thickness d_s and refractive index n_s suspended on free space. The squared magnitude of s is a function of f_{THz}, whose value is given by

$$|s(f_{THz})|^2 = \left(\frac{|r(f_{THz})|}{|t(f_{THz})|}\right)^2 = \left(\frac{2\sqrt{R}}{1-R}\right)^2 \sin^2(k_s d_s) \quad (9)$$

where $r(f_{THz})$ is the field reflection coefficient exhibited by the slab, $t(f_{THz})$ its field transmission coefficient, $R = \frac{n_s-1}{n_s+1}$, $k_s = \frac{2\pi n_s f_{THz}}{c}$. The fitting is done independently for each of the ratios obtained for the two distinct ports. The details of the algorithms used for the fitting are discussed in Appendix 1. The estimated thickness using the data from port 1 was $d_{s,1} = 226.56$ μm, and the refractive index $n_{s,1} = 2.014$, while the estimated thickness using the data from port 2 was $d_{s,2} = 225.66$ μm, and the refractive index $n_{s,2} = 2.003$. Both values match very well with the 220 ± 5 μm thickness measured using a caliper, and with the refractive indices reported in the literature [23].

B. APPLICATION 2: CHARACTERIZATION OF A TERAHERTZ DBR

Fig. 7 shows the magnitude and phase of the four scattering parameters of the in-house fabricated DBR measured using the same settings, calibration procedure and post-processing techniques as before. The DBR consisted of three 524-μm thick layers of highly resistive silicon, with an air spacing of 150 μm each. According to its theoretical response, the main stopband should be centered at 0.623 THz with a 3-dB
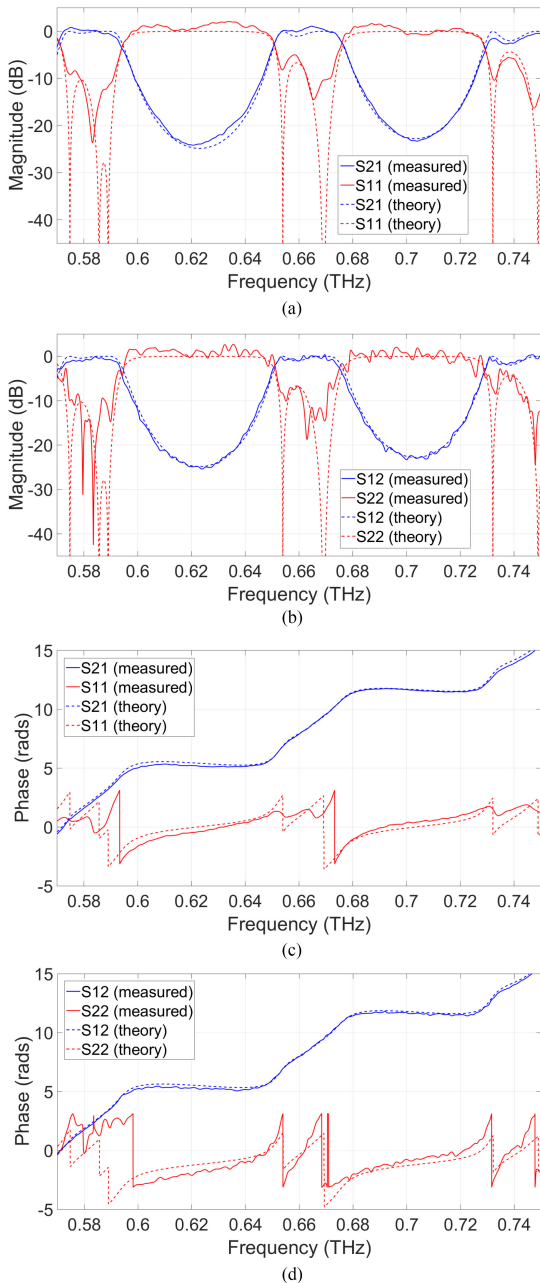
FIGURE 7. Comparison between the measured scattering parameters of the DBR after the filtering process, and the theoretically calculated scattering parameters. (a) Amplitude comparison obtained for port 1. (b) Amplitude comparison obtained for port 2. (c) Phase comparison obtained for port 1. (d) Phase comparison obtained for port 2.

bandwidth of around 0.056 THz. We measured that stopband, and the adjacent one, theoretically centered at 0.703 THz.

In general, there is good agreement between the measured and the theoretical response. There are only two significant discrepancies. The first one is the rather high magnitude of the measured reflection coefficients for the passbands of the DBR, in particular, between 0.65 and 0.67 THz. The second significant discrepancy is the phase of the reflection coefficients for exactly the same frequency range. Indeed, some of the measured phase jumps within that range equal to 2π,

which would have resulted in their removal when unwrapping the phase. Thus, we did not unwrap the phase of the measured reflection coefficients for that range. Otherwise, a meaningful comparison between the theoretical phase and the measured phase would have been difficult.

The most likely cause for these discrepancies is the calibration procedure. Given the high degree of frequency selectivity of the SUT, even small tilts of the calibration tool might have given rise to significant changes in the measured response, as it occurs in a gratings. Additionally, a slight mismatch between the physical reference plane of the sample and that of the gold mirror could certainly impact the measured phase of the reflection coefficients. Still, the measured scattering parameters allowed for a useful characterization of the in-house built DBR.

V. CONCLUSION

We have demonstrated a free-space coupled CW optoeletronic VNA operating continuously from 0.1 to 1 THz. We obtained a maximum dynamic range of around 80 dB in transmission mode, achieved at 0.1 THz and with an integration time of 100 ms. While we obtained a maximum dynamic range of 90 dB in reflection mode, also with an integration time of 100 ms (corresponding to an equivalent noise bandwidth of 0.5 Hz).

We have shown that the VNA can be used to accurately determine the refractive index and the thickness of bulk materials and also to characterize terahertz components with a high resolution. A very important aspect for the successful accomplishment of any of these applications is the digital post-processing techniques, given the amount of undesired reflections inherent to any free-space terahertz setup, regardless of its optoelectronic or purely electronic nature.

The demonstrated free-space VNA can be right away used with the approach presented in [14], [15] to also characterize transmission-line-coupled components such as transistors. This would finally allow to overcome the frequency and cost limitations imposed by terahertz VNAs based on frequency extenders for the characterization of any type of components within 0.1 THz and 1 THz and beyond.

APPENDIX: FITTING ALGORITHM

The fitting algorithm is based on an iterative error minimization process. An initial guess, n_{est} and d_{est}, is first obtained by fitting the measured data to $|s|$ using non-linear least squares. This guess is then used as the starting point of the iterative process.

The iterative process consists of three different optimization steps:

1) Using only the periodicity of the data to be fitted, a new optical thickness d_{opt} is obtained (this optical thickness, multiplied by $\frac{2\pi f_{THz}}{c}$, represents the argument of the sine function of (9)). New guesses, $n_{est,1}$ and d_{est}, and n_{est} and $d_{est,1}$, are then calculated using

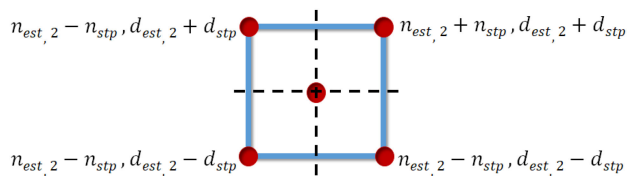$$n_{est,1} = \frac{d_{opt}}{d_{est}} \qquad (10)$$

FIGURE 8. Graphical depiction of the coarse 'global' minimization strategy performed in each iteration of the loop run at step 2.

and

$$d_{est,1} = \frac{d_{opt}}{n_{est}}. \tag{11}$$

The errors obtained with the two new guesses are then compared with the error obtained with the initial guess, and the one with smallest errors becomes the new guess.

2) A loop is started in which four new guesses are tried sequentially in every loop iteration. The four guesses are: $n_{est,2} + n_{stp}$ and $d_{est,2} + d_{stp}$, $n_{est,2} - n_{stp}$ and $d_{est,2} + d_{stp}$, $n_{est,2} - n_{stp}$ and $d_{est,2} - d_{stp}$, and $n_{est,2} + n_{stp}$ and $d_{est,2} - d_{stp}$, as shown in Fig. 8. The steps, n_{stp} and d_{stp}, can be chosen as small as desired. but they must remain constant through the whole process.

At each iteration, the error of all the four guesses is compared to the error of the initial guess, and the one with the smallest error becomes the new guess, $n_{est,3}$ and $d_{est,3}$. The loop is repeated until the error cannot be minimized anymore.

3) The previous step can be seen as a coarse 'global' minimization process to avoid getting stuck in a local in minima. The fine 'local' minimization process is performed using a 1D-gradient-descent like approach with a fixed step size. In this way, the error in $n_{est,3}$ and $d_{est,3}$ is minimized separately. Once the errors have been minimized, the process starts again from step 1, using this error-minimized guess as $n_{est,1}$ and $d_{est,1}$.

The whole process is repeated until the error does not decrease substantially anymore, or when the error starts to increase. Since this usually occurs not before ten iterations, this is set as the maximum number of iterations.

ACKNOWLEDGMENT

REFERENCES

[1] S. Preu *et al.*, "Tunable, continuous-wave terahertz photomixer sources and applications," *J. Appl. Phys.*, vol. 109, 2011, Art no. 0 61301.

[2] S. Preu, "A unified derivation of the terahertz spectra generated by photoconductors and diodes," *J. Infrared, Millimeter, THz Waves*, vol. 35, pp. 998–1010, 2014.

[3] U. Nandi *et al.*, "1550-nm driven ErAs:In(Al)GaAs photoconductor-based terahertz time domain system with 6.5 THz bandwidth," *J. Infrared, Millimeter, THz Waves*, vol. 39, no. 4, pp. 340–348, 2018.

[4] R. Kohlhaas *et al.*, "Fiber coupled transceiver with 6.5 THz bandwidth for terahertz time-domain spectroscopy in reflection geometry," *Sensors*, vol. 20, no. 9, pp. 2616:1–2616:12, 2020.

[5] L. Liebermeister *et al.*, "Optoelectronic frequency-modulated continuous-wave terahertz spectroscopy with 4 THz bandwidth," *Nature Commun.*, vol. 12, pp. 1071:1–1071:10, 2021.

[6] A. R. Criado *et al.*, "Continuous-wave sub-THz photonic generation with ultra-narrow linewidth, ultra-high resolution, full frequency range coverage and high long-term frequency stability," *IEEE Trans. THz Sci. Technol.*, vol. 3, no. 4, pp. 461–471, Jul. 2013.

[7] A. D. J. F. Olvera *et al.*, "Frequency selective optoelectronic downconversion of a terahertz pulse using ErAs: In(Al)GaAs photoconductors," *IEEE Access*, vol. 9, pp. 95391–95400, 2021.

[8] S. Yokoyama *et al.*, "Terahertz spectrum analyzer based on a terahertz frequency comb," *Opt. Exp.*, vol. 16, no. 17, pp. 13052–13061, 2008.

[9] G. Hu *et al.*, "Measurement of absolute frequency of continuous-wave terahertz radiation in real time using a free-running, dual-wavelength mode-locked, erbium-doped fibre laser," *Sci. Rep.*, vol. 7, pp. 42082:1–42082:11, 2017.

[10] F. R. Faridi and S. Preu, "Characterization of a terahertz isolator using a 1.5 port vector spectrometer," in *Proc. 44th Int. Conf. Infrared, Millimeter, THz Waves*, Paris, France, 2019 pp. 1–2.

[11] M. Mueh *et al.*, "Calibration technique for THz time-domain spectrometers enabling vectorial scattering parameter measurements," *Microw. Wireless Compon. Lett.*, vol. 31, no. 6, pp. 805–807, Jun. 2021.

[12] F. R. Faridi and S. Preu, "Pulsed free space two-port photonic vector network analyzer with up to 2 THz bandwidth," *Opt. Exp.*, vol. 29, no. 8, pp. 12278–12291, 2021.

[13] A. Jimenez-Saez *et al.*, "Frequency-coded mm-wave tags for self-localization system using dielectric resonators," *J. Infrared, Millimeter, THz Waves*, vol. 41, pp. 908–925, 2020.

[14] C. Caglayan, G. C. Trichopoulos, and K. Sertel, "Non-contact probes for on-wafer characterization of sub-millimeter-wave devices and integrated circuits," *IEEE Trans. Microw. Theory Techn.*, vol. 61, no. 11, pp. 2791–2801, Nov. 2014.

[15] Y. Karisan *et al.*, "Lumped-element equivalent-circuit modeling of millimeter-wave HEMT parasitics through full-wave electromagnetic analysis," *IEEE Trans. Microw. Theory Techn.*, vol. 64, no. 5, pp. 1419–1430, May 2016.

[16] M. Hiebel, *Fundmentals of Vector Network Analyzers*. Munich, Germany: Rohde & Schwarz GmbH & Co., 2008.

[17] A. D. J. Fernandez Olvera, B. L. Krause, and S. Preu, "A true optoelectronic spectrum analyzer for the sub-terahertz range with Hz resolution," *IEEE Access*, vo. 9, pp. 114339–114347, 2021.

[18] D. W. Vogt, M. Erkintalo, and R. Leonhardt, "Coherent continuous wave terahertz spectroscopy using Hilbert transform," *J. Infrared, Millimeter, THz Waves*, vol. 40, pp. 524–534, 2019.

[19] A. Ingar Romero *et al.*, "Visualizing nanometric structures with sub-millimeter waves," *Nature Commun.*, to be published, 2021.

[20] A. J. Deninger *et al.*, "2.75 THz tuning with a triple-DFB laser system at 1550 nm and InGaAs photomixers," *J. Infrared, Millimeter, THz Waves*, vol. 36, pp. 269–277, 2015.

[21] A. D. J. F. Olvera *et al.*, "International System of Units (SI) traceable noise-equivalent power and responsivity characterization of continuous wave ErAs:InGaAs photoconductive terahertz detectors," *Photonics*, vol. 6, no. 1, pp. 15:1–15:9, 2019.

[22] B. Will and I. Rolfes, "A new approach on broadband calibration methods for free space applications," in *Proc. IEEE/MTT-S Int. Microw. Symp.*, Montreal, QC, Canada, 2012, pp. 1–3.

[23] C. Davies *et al.*, "Temperature-dependent refractive index of quartz at terahertz frequencies," *J. Infrared, Millimeter, THz Waves*, vol. 39, pp. 1236–1248, 2018.